Supplementary Information

Hybridization-Tuned Dual-Chain Conjugated Polythioether Quinones for High-Energy Rechargeable Magnesium Batteries

Hongda Gui[a], Ze Wang[a], Yuliang Cao[b], Fei Xu[a,*]

[a] Key Laboratory of Hydraulic Machinery Transients, Ministry of Education, School of Power and Mechanical Engineering, Wuhan University, Wuhan 430072, China.
[b] Hubei Key Lab of Electrochemical Power Sources, College of Chemistry & Molecular Science, Wuhan University, Wuhan 430072, China.

* E-mail: Fei Xu (xufei2058@whu.edu.cn)

Table S1. Different molecular configurations of 26PBQS and their energy comparison.

Molecular Configuration	*Energy (a.u.)*
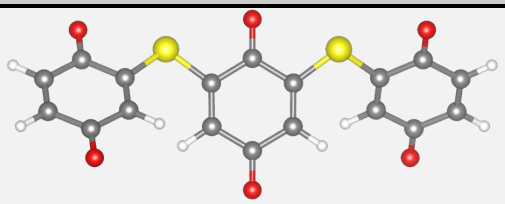	−1938.777442
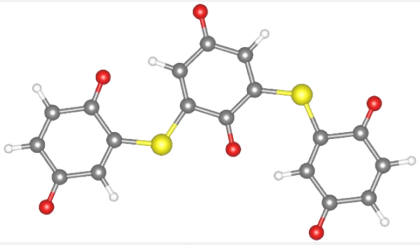	−1938.750266
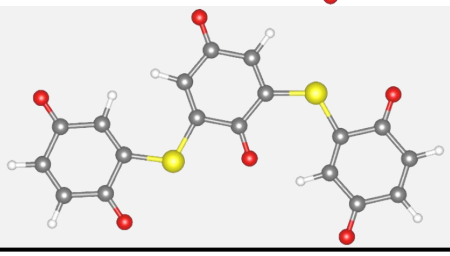	−1938.758316

Table S2. ELF isosurfaces (isovalue = 0.5) of 25PBQS, 26PBQS, 2356PBQS.

Molecule	*ELF isosurfaces*		
25PBQS	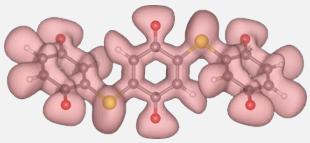		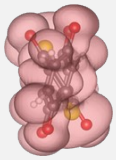
26PBQS	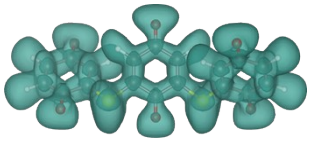	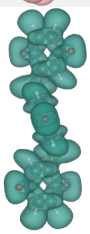	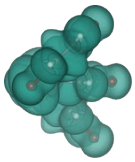
2356PBQS	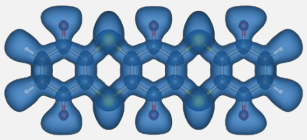		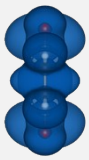

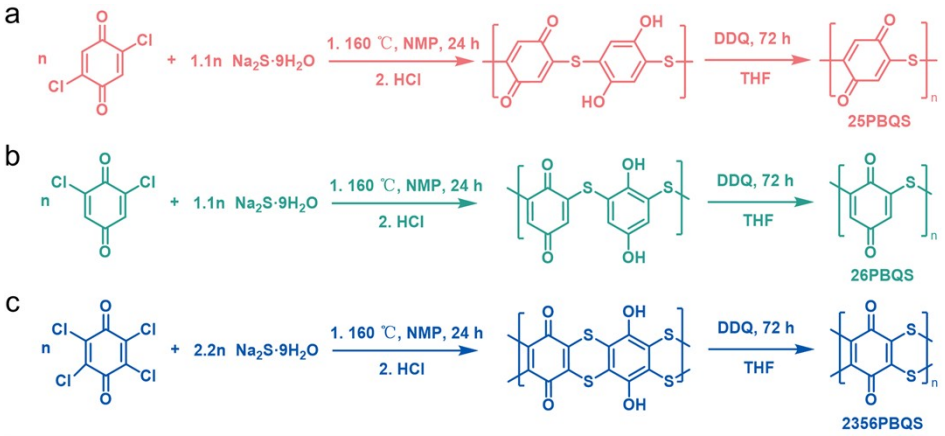

Fig. S1. Synthetic procedures of 25PBQS, 26PBQS, and 2356PBQS.

The polymer synthesis protocol was adapted from reported literature methods with critical modifications.[1–3] Owing to the strong oxidative nature of benzoquinone, undesired redox side reactions with sulfide anions were observed. Comparative studies of various sulfides (Li_2S, Na_2S, and K_2S) and reactant ratios revealed that $Na_2S·9H_2O$—owing to its relatively low solubility—minimized side reactions and maximized polymerization efficiency. A 10% molar excess of $Na_2S·9H_2O$ was required to ensure sufficient sulfur participation in monomer activation, with iterative optimization confirming this ratio yielded products with the highest polymerization degree and electrochemical activity. Prior to reaction, sonication was employed to enhance the dispersion and dissolution of $Na_2S·9H_2O$ in NMP, facilitating the nucleophilic substitution reaction while suppressing parasitic side pathways.

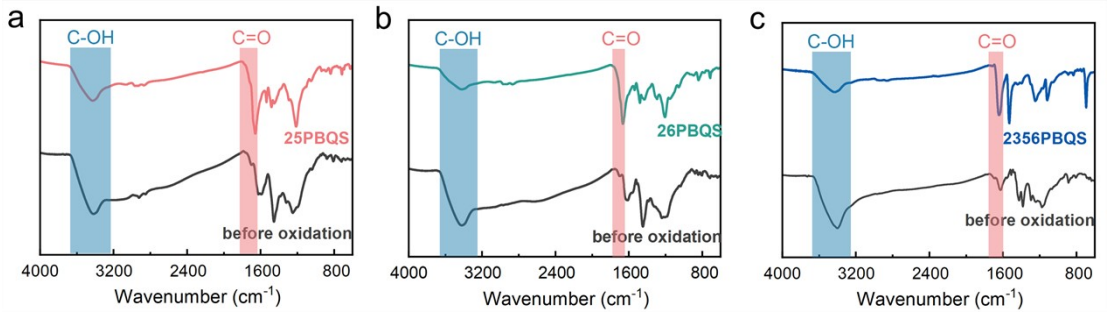

Fig. S2. FTIR spectra of (a) 25PBQS, (b) 26PBQS, and (c) 2356PBQS products before and after oxidation.

The persistence of the C–OH peak suggests that interference from ambient moisture cannot be fully excluded, which is in line with previous reports. [2–3]

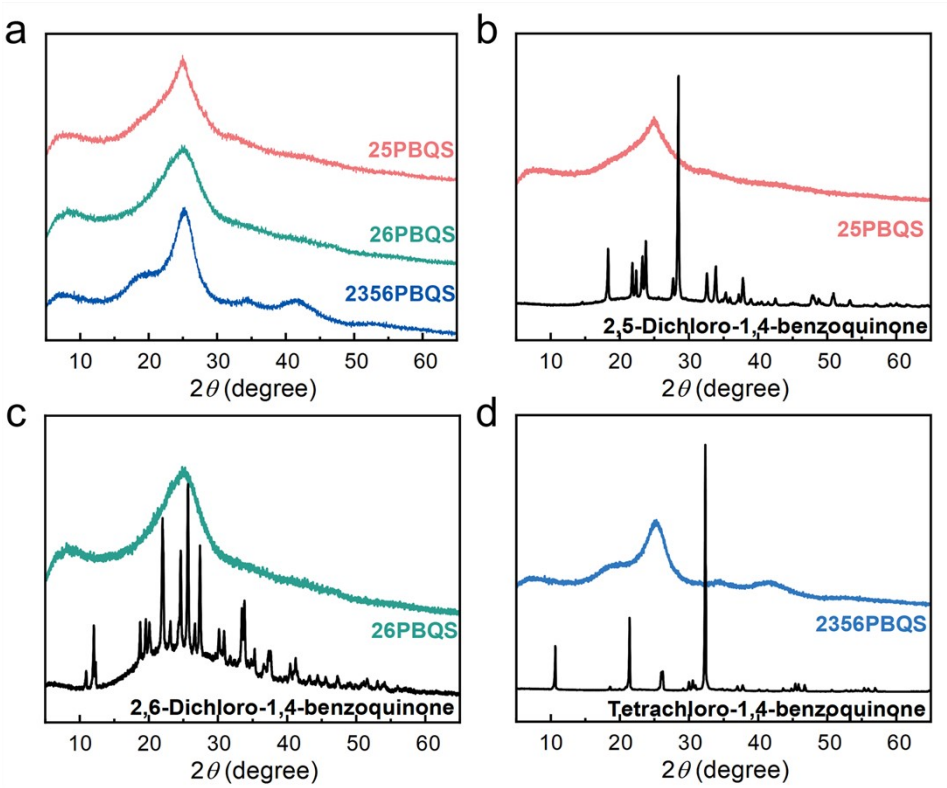

Fig. S3. XRD patterns of (a) 25PBQS, 26PBQS and 2356PBQS, (b) 25PBQS and 2,5-dichloro-1,4-benzoquinone, (c) 26PBQS and 2,6-dichloro-1,4-benzoquinone, (d) 2356PBQS and tetrachloro-1,4-benzoquinone.

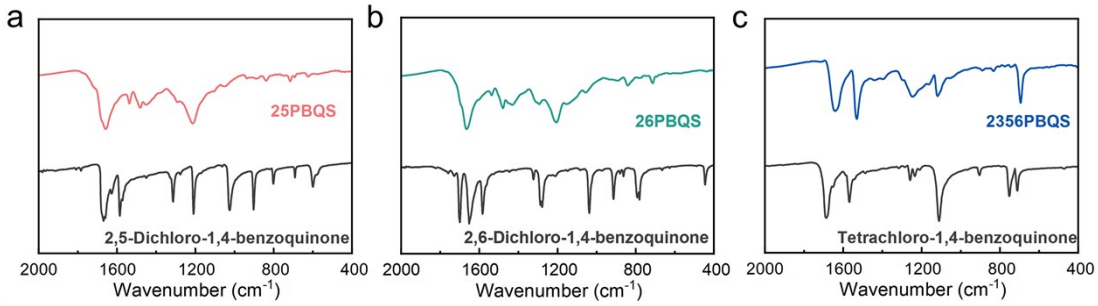

Fig. S4. FTIR spectra of (a) 25PBQS and 2,5-dichloro-1,4-benzoquinone, (b) 26PBQS and 2,6-dichloro-1,4-benzoquinone, (c) 2356PBQS and tetrachloro-1,4-benzoquinone.

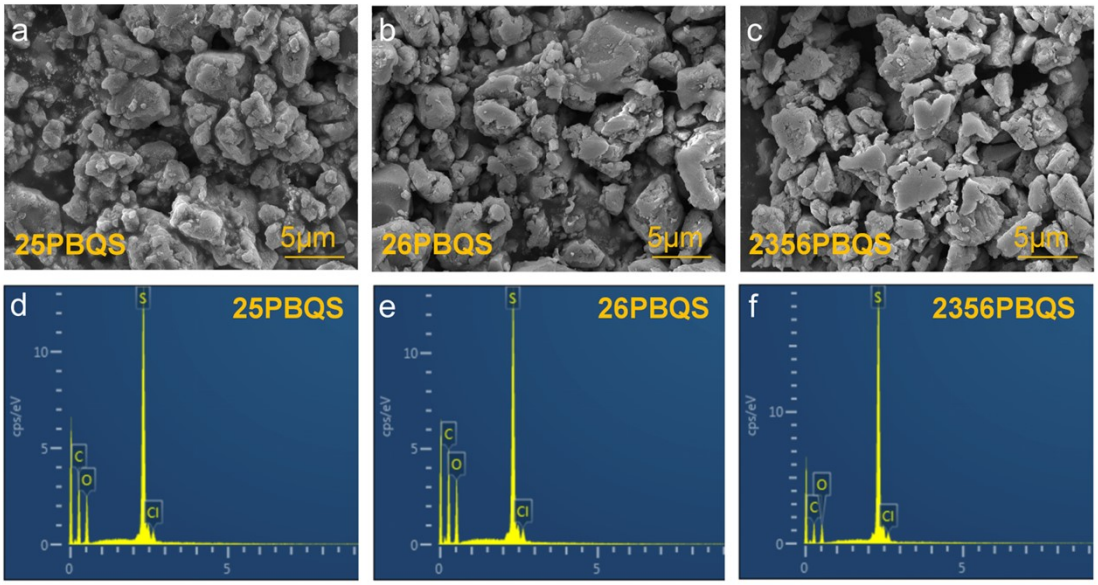

g

Element	Atomic Fraction		
	25PBQS	*26PBQS*	*2356PBQS*
C	71.42	70.20	65.52
O	19.41	21.93	16.17
S	8.70	7.41	17.46
Cl	0.48	0.46	0.85

h

Materials	Average Polymerization Degree
25PBQS	37.3
26PBQS	33.2
2356PBQS	42.1

Fig. S5. SEM images of (a) 25PBQS, (b) 26PBQS, and (c) 2356PBQS. EDS spectra of (d) 25PBQS, (e) 26PBQS, and (f) 2356PBQS. (g) Elemental compositions and (h) polymerization degree estimation.

The polymerization degree was estimated using the following equation derived from EDS data:

$$DP = \frac{S + 0.5Cl}{Cl} \times 2$$

Where S is the element proportion of S element and Cl is the element proportion of Cl element.

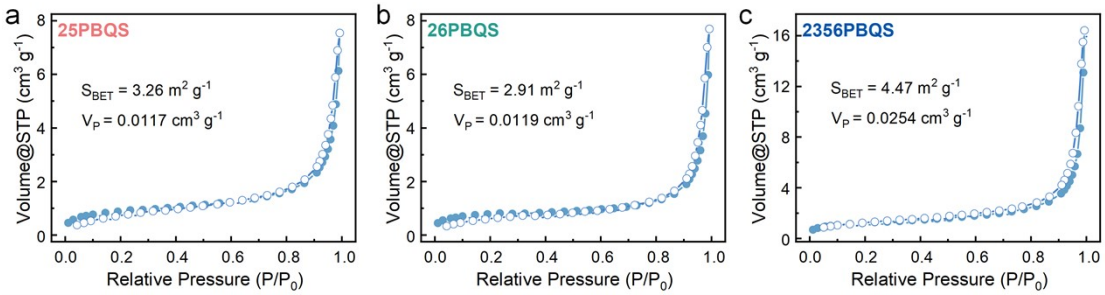

Fig. S6. N_2 adsorption and desorption isotherms of (a) 25PBQS, (b) 26PBQS, and (c) 2356PBQS.

2356PBQS exhibits the largest specific surface area and highest pore volume among the three materials.

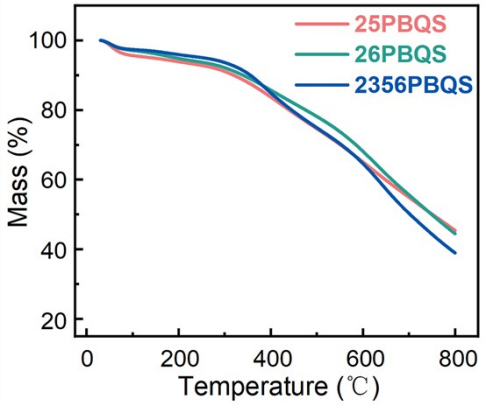

Fig. S7. TGA profiles of 25PBQS, 26PBQS and 2356PBQS.

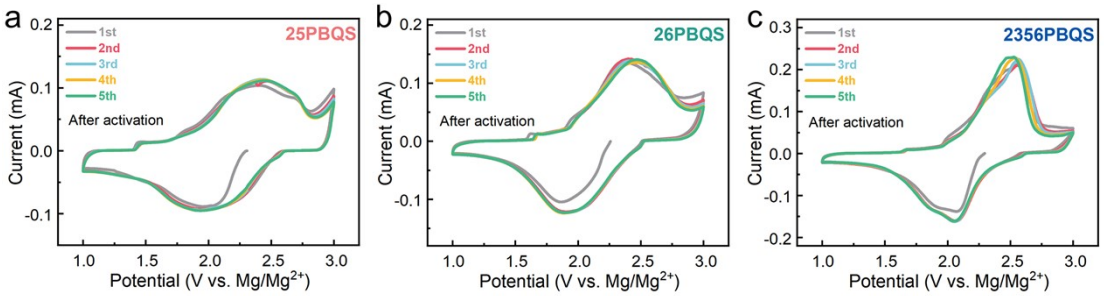

Fig. S8. CV curves (after activation, at 0.1 mV s^{-1}) of (a) 25PBQS, (b) 26PBQS, and (c) 2356PBQS.

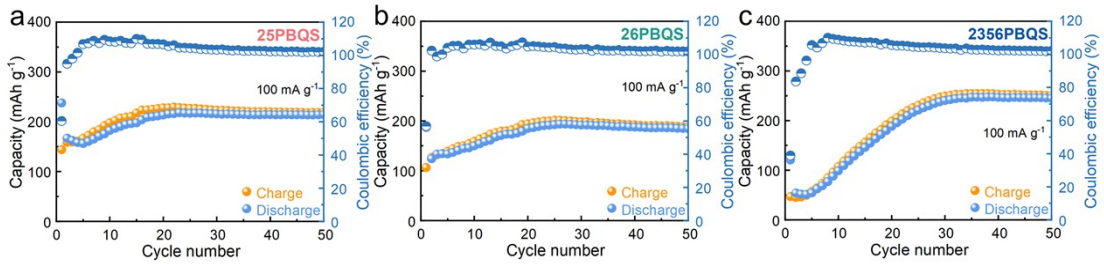

Fig. S9. Cycling performances (100 mA g^{-1}) of (a) 25PBQS, (b) 26PBQS, and (c) 2356PBQS.

Table S3. Electrochemical performance of typical high-performance cathode materials for RMBs.

Compound	*Electrolyte*	*Current Density*	*Discharge Capacity (mAh g^{-1})*	*Reduction peak (V)*
d-PAQS[4]	0.25 M $Mg(TFSI)_2$-$MgCl_2$/DME	0.2 C	194	1.48
PAQI-P26[5]	0.5 M $Mg(TFSI)_2$-$MgCl_2$/DME	50 mA g^{-1}	184	1.5
PAQI-N26[5]	0.5 M $Mg(TFSI)_2$-$MgCl_2$/DME	50 mA g^{-1}	142	1.5
2,6-PBQS[6]	0.25 M $Mg(TFSI)_2$-$MgCl_2$/DME	50 mA g^{-1}	165	1.6
PBQPy[7]	0.5 M $Mg[B(HFIP)_4]_2$/ G2-DME	100 mA g^{-1}	197	1.6
PDAAQ[8]	0.25 M $Mg(TFSI)_2$-$MgCl_2$/DME	50 mA g^{-1}	205	1.45
PI-SS[9]	0.25 M $Mg(TFSI)_2$-$MgCl_2$/DME	50 mA g^{-1}	155	1.4
PI1/CNTs[10]	$Mg(HMDS)_2$-$4MgCl_2$/2THF-$PP_{14}TFSI$	183 mA g^{-1}	132	1.6
Cu_3VSe_4[11]	0.25 M $Mg(TFSI)_2$-$MgCl_2$/DME	200 mA g^{-1}	251	0.85
$Cu_{2-x}Se$[12]	$Mg(HMDS)_2$- $AlCl_3$/DME	100 mA g^{-1}	222	0.92
Cu_3VS_4[13]	0.25 M $Mg(TFSI)_2$-$MgCl_2$/DME	100 mA g^{-1}	350	0.89

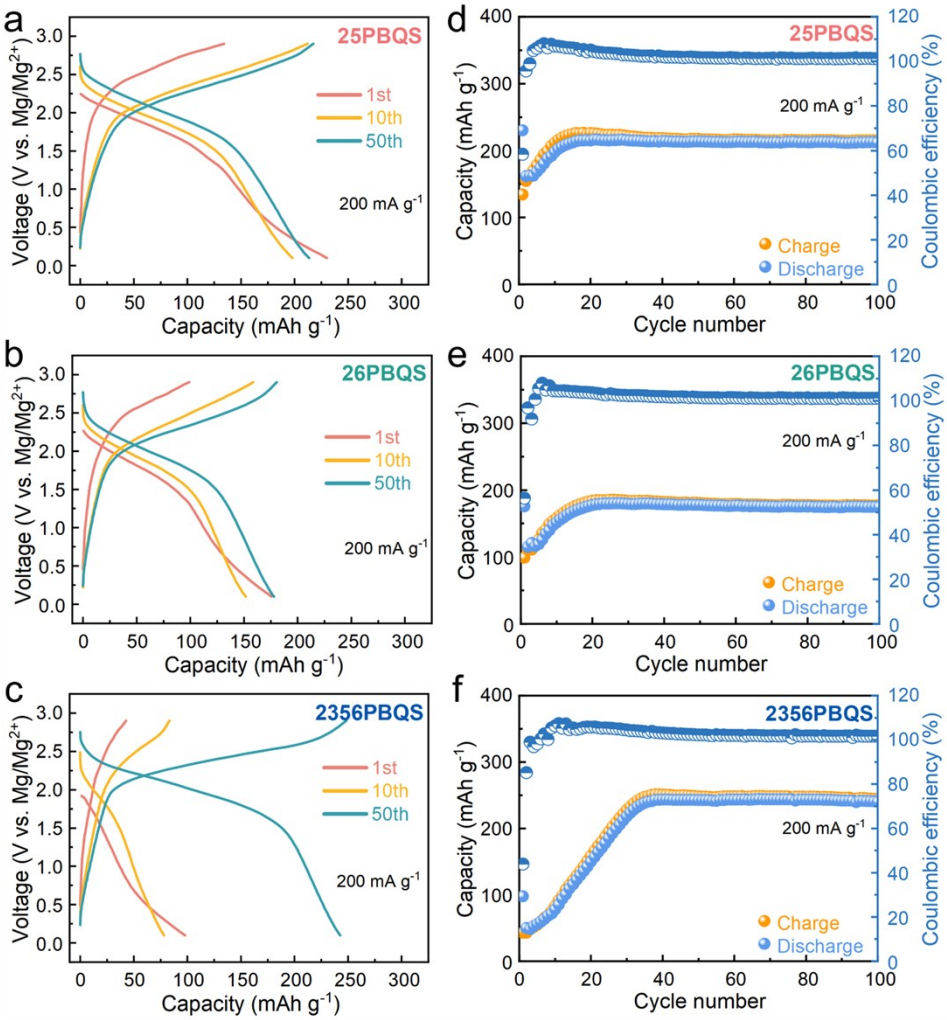

Fig. S10. (a–c) Charge-discharge profiles and (d–f) cycling performance of 25PBQS, 26PBQS, and 2356PBQS with $Mg(TFSI)_2$-$MgCl_2$/DME electrolyte at 200 mA g^{-1}.

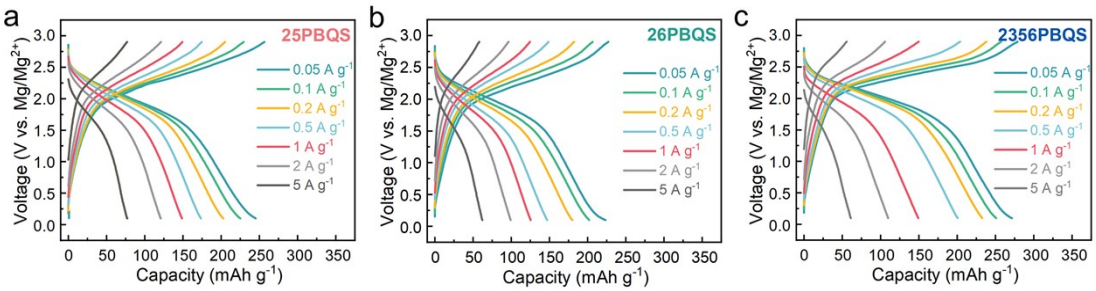

Fig. S11. Charge-discharge profiles of (a) 25PBQS, (b) 26PBQS, and (c) 2356PBQS at different current densities with $Mg(TFSI)_2$-$MgCl_2$/DME electrolyte.

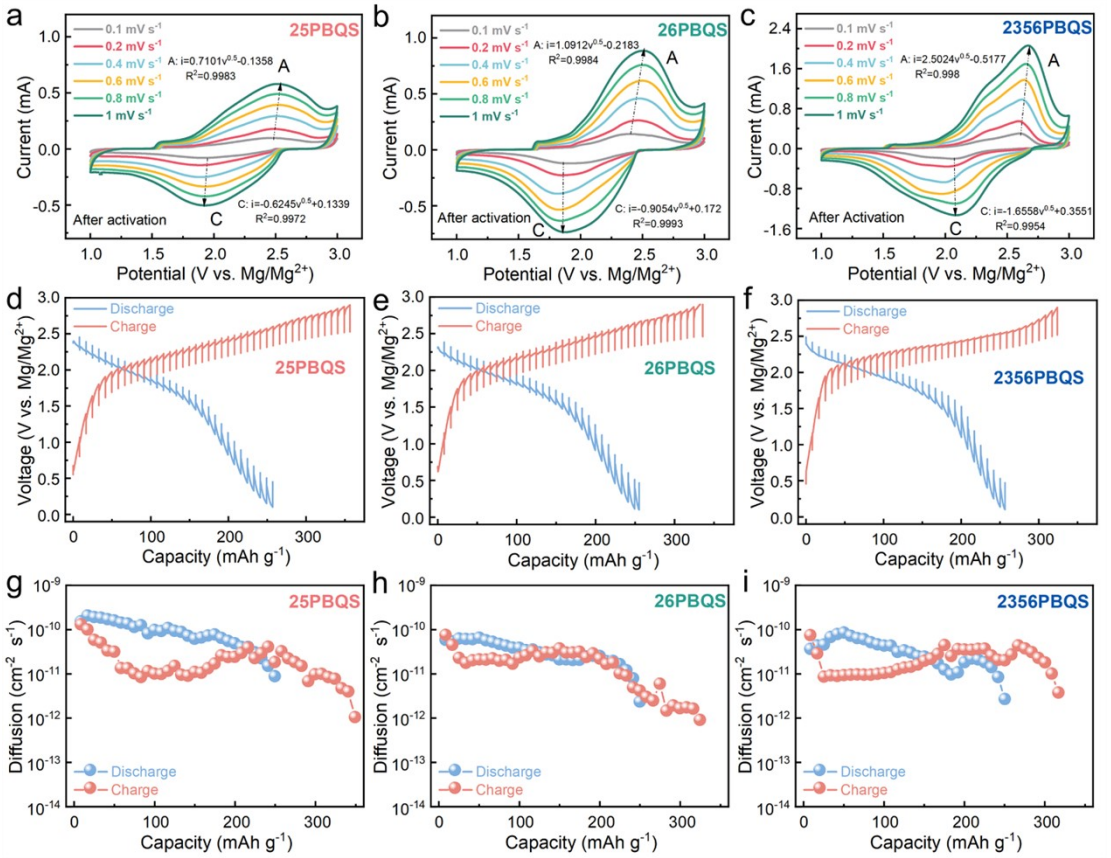

Fig. S12. (a–c) CV curves at different scan rates (after activation), (d–f) GITT profiles, and (g–i) corresponding Mg^{2+} diffusion coefficients of 25PBQS, 26PBQS, and 2356PBQS in $Mg(TFSI)_2$-$MgCl_2$/DME electrolyte.

Table S4. Specific energy density and power density of Mg‖25PBQS cell in $Mg(TFSI)_2$-$MgCl_2$/DME electrolyte.

Current Density ($mAh\ g^{-1}$)	C_c ($mAh\ g^{-1}$)	C_a ($mAh\ g^{-1}$)	E (V)	Specific Energy ($Wh\ kg^{-1}$)	Specific Power ($Wh\ kg^{-1}$)
50	246.90	2205	1.579	350.6	77.9
100	227.35	2205	1.607	331.2	160.7
200	206.42	2205	1.619	305.59	323.9
500	175.14	2205	1.633	264.96	816.4
1000	149.21	2205	1.613	225.42	1612.6
2000	122.84	2205	1.545	179.77	3090.5
5000	80.35	2205	1.403	108.77	7016.2

C_c is cathode specific capacity, C_a is anode specific capacity, E is the average discharge voltage. Specific energy is calculated according to the following equation:[14]

$$Specific\ energy\ density = \frac{E}{\frac{1}{C_a} + \frac{1}{C_c}}$$

Table S5. Specific energy density and power density of Mg‖26PBQS cell in $Mg(TFSI)_2$-$MgCl_2$/DME electrolyte.

Current Density ($mAh\ g^{-1}$)	C_c ($mAh\ g^{-1}$)	C_a ($mAh\ g^{-1}$)	E (V)	Specific Energy ($Wh\ kg^{-1}$)	Specific Power ($Wh\ kg^{-1}$)
50	223.34	2205	1.551	314.54	77.7
100	202.56	2205	1576	292.38	157.6
200	178.99	2205	1578	261.24	315.6
500	149.06	2205	1.567	218.84	783.7
1000	125.44	2205	1.531	181.74	1531.3
2000	99.16	2205	1.467	139.22	2934.2
5000	55.59	2205	1.297	75.26	6485.1

Table S6. Specific energy density and power density of Mg‖2356PBQS cell in $Mg(TFSI)_2$-$MgCl_2$/DME electrolyte.

Current Density (mAh g^{-1})	***C_c (mAh g^{-1})***	***C_a (mAh g^{-1})***	***E (V)***	***Specific Energy (Wh kg^{-1})***	***Specific Power (Wh kg^{-1})***
50	271.91	2205	1.662	402.30	83.1
100	250.98	2205	1.673	376.92	167.3
200	235.06	2205	1.695	360.15	339.1
500	200.52	2205	1.642	301.77	820.9
1000	153.82	2205	1.586	228.04	1585.9
2000	100.79	2205	1.509	144.10	3017.1
5000	61.10	2205	1.235	73.44	6176.8

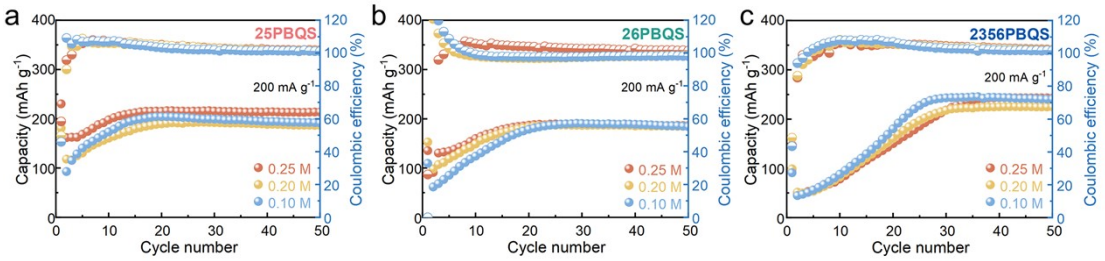

Fig. S13. Cycling performances of (a) 25PBQS, (b) 26PBQS and (c) 2356PBQS in $Mg(TFSI)_2$-$MgCl_2$/DME electrolytes with different concentrations.

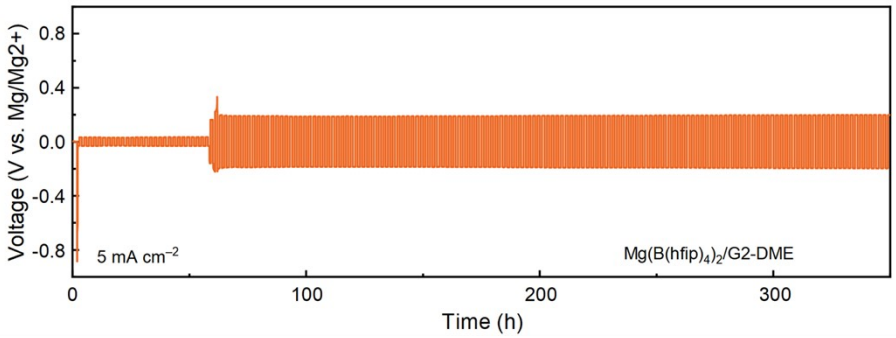

Fig. S14. Symmetric Mg plating/stripping performance of $Mg(B(hfip)_4)_2$/G2-DME electrolyte.

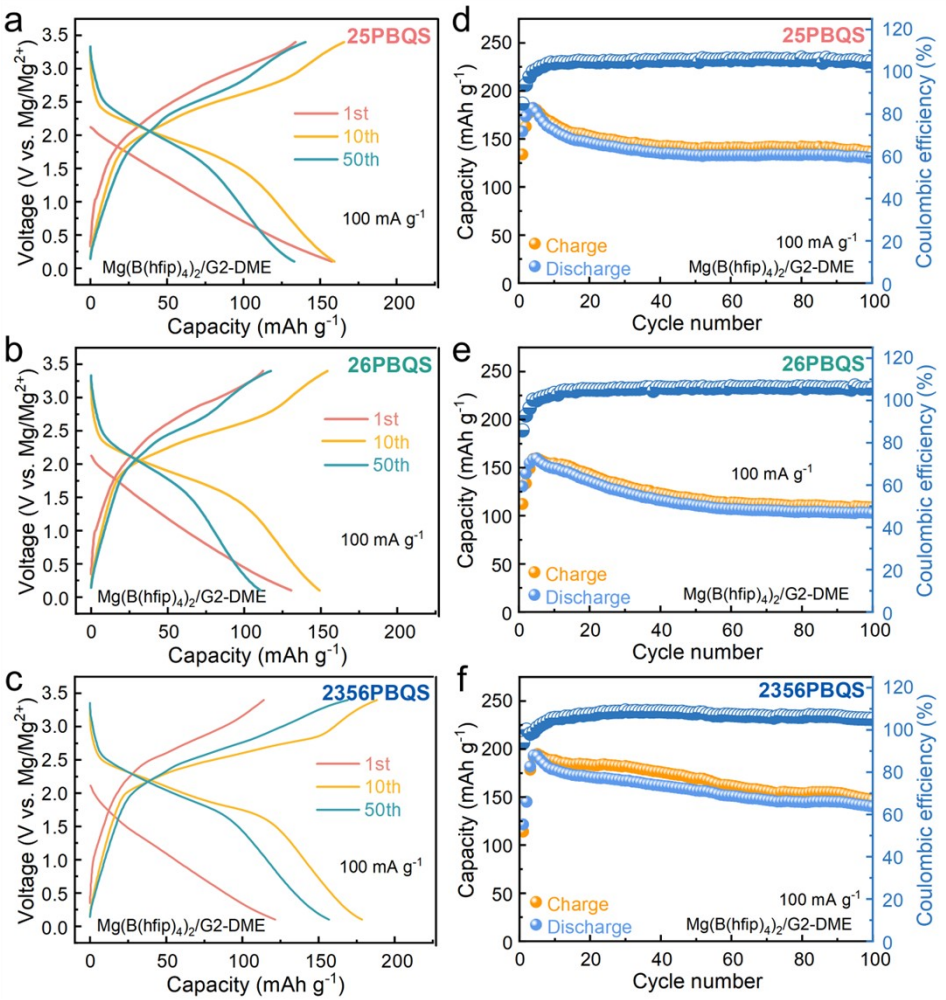

Fig. S15. (a–c) Charge-discharge profiles and (d–f) cycling performance of 25PBQS, 26PBQS, and 2356PBQS with $Mg(B(hfip)_4)_2$/G2-DME electrolyte at 100 mA g^{-1}.

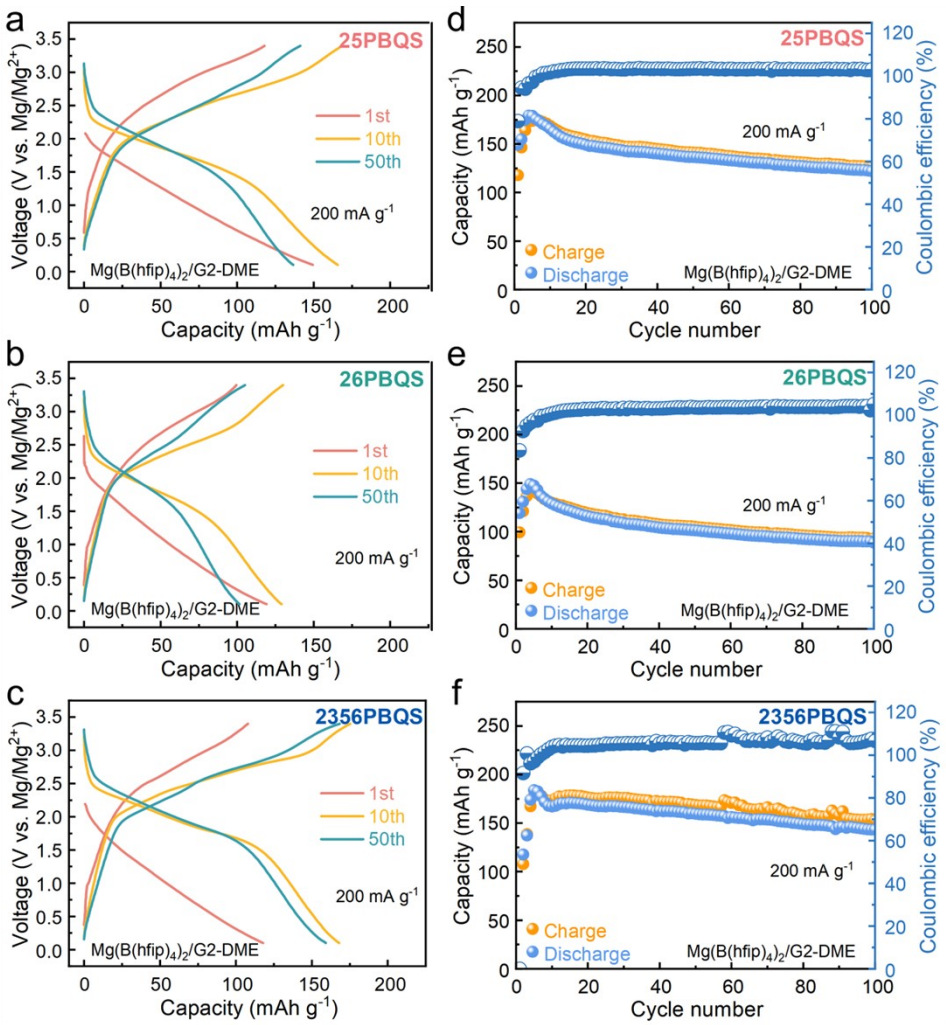

Fig. S16. (a–c) Charge-discharge profiles and (d–f) cycling performance of 25PBQS, 26PBQS, and 2356PBQS with $Mg(B(hfip)_4)_2$/G2-DME electrolyte at 200 mA g^{-1}.

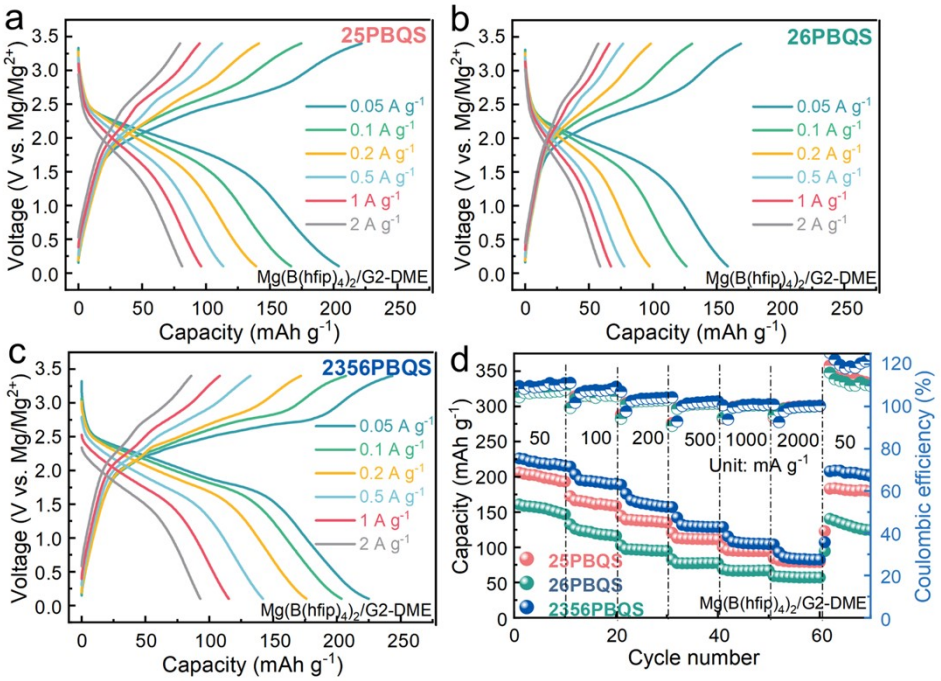

Fig. S17. Charge-discharge profiles of (a) 25PBQS, (b) 26PBQS, and (c) 2356PBQS at different current densities, and (d) rate performance with $Mg(B(hfip)_4)_2$/G2-DME electrolyte.

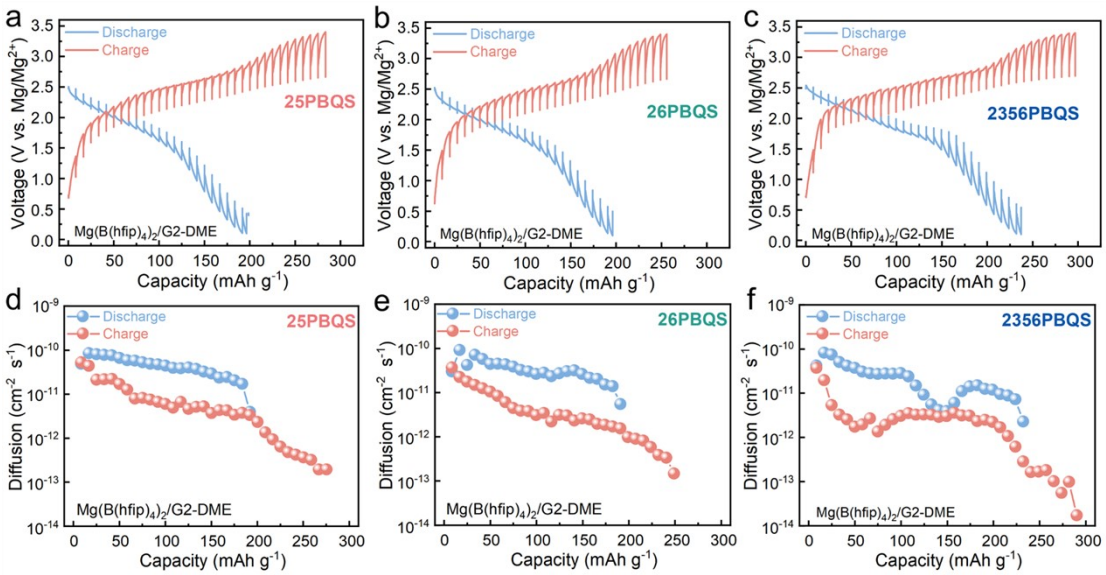

Fig. S18. (a–c) GITT profiles, and (d–f) corresponding Mg^{2+} diffusion coefficients of 25PBQS, 26PBQS, and 2356PBQS with $Mg(B(hfip)_4)_2$/G2-DME electrolyte.

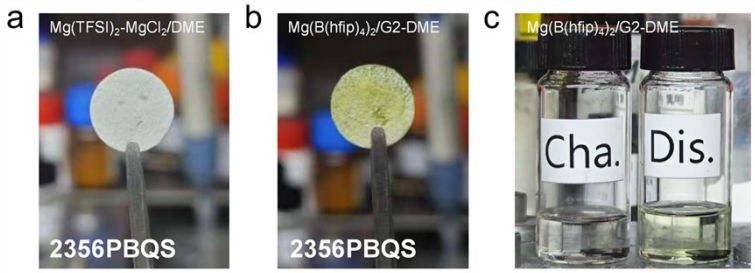

Fig. S19. Post-cycling analysis of the Mg‖2356PBQS cell: (a) Separator morphology in $Mg(TFSI)_2$-$MgCl_2$/DME electrolyte. (b) Separator and (c) catholyte residues in $Mg(B(hfip)_4)_2$/G2-DME electrolyte.

In the $Mg(TFSI)_2$-$MgCl_2$/DME electrolyte, the cell separator remained white after cycling (Figure S18a), indicating negligible dissolution of 2356PBQS during charge/discharge processes. The inorganic salts in the electrolyte suppresses dissolution (due to the "like dissolves like" principle). In contrast, the separator in the $Mg[B(hfip)_4]_2$/G2-DME electrolyte system exhibited a yellow-green color, signifying possible material dissolution (Figure S18b). Furthermore, charged-state and discharged-state cathodes were immersed in DME (Figure S18c). Only the discharged-state 2356PBQS cathode altered the DME color, demonstrating that dissolution predominantly involves discharged-state 2356PBQS. Additionally, this material dissolution enables partial activation to proceed in the liquid phase, thereby accelerating the overall activation process.

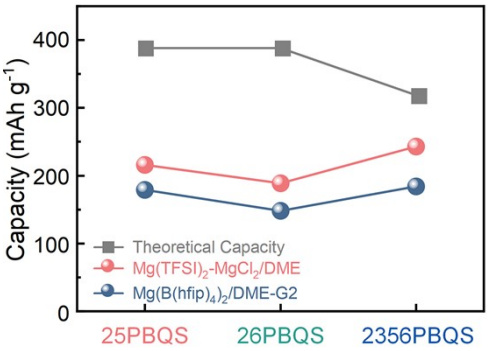

Fig. S20. Comparative specific capacities of 25PBQS, 26PBQS, and 2356PBQS using $Mg(TFSI)_2$-$MgCl_2$/DME and $Mg(B(hfip)_4)_2$/G2-DME electrolytes (200 mA g^{-1}).

Table S7. Elemental composition of 2356PBQS at the charge and discharge states of the 35th cycle using $Mg(TFSI)_2$-$MgCl_2$/DME electrolyte.

Charge		***Discharge***	
Element	**Atomic Fraction (%)**	**Element**	**Atomic Fraction (%)**
C	92.4	C	81.9
O	3.7	O	9.1
S	3.1	S	5.7
Mg	0.7	Mg	2.9
Cl	0.1	Cl	0.4

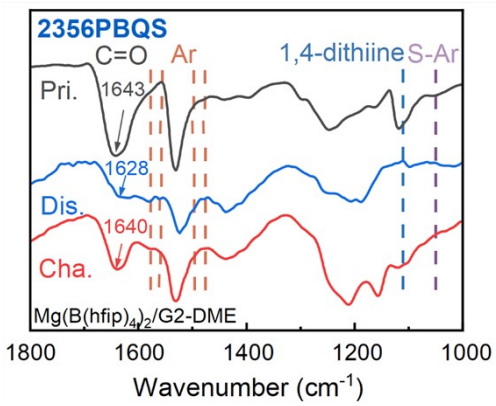

Fig. S21. FTIR spectra of 2356PBQS at the charge and discharge states of the 4th cycle with $Mg(B(hfip)_4)_2$/G2-DME electrolyte.

Table S8. LOL-Π isosurfaces (isovalue = 0.4) of 25PBQS, 26PBQS, 2356PBQS, and their respective reduction states.

Molecule	*Oxidation State*	*Two-electron Reduced State*	*Four-electron Reduced State*	*Six-electron Reduced State*
25PBQS	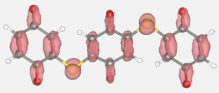	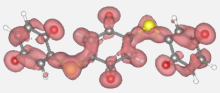	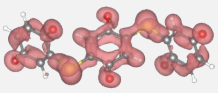	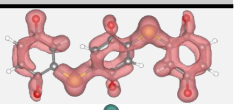
26PBQS	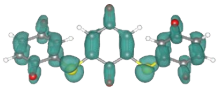	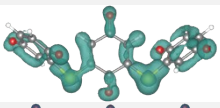	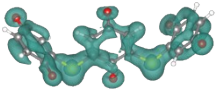	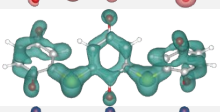
2356PBQS	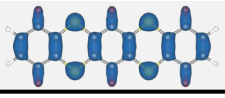	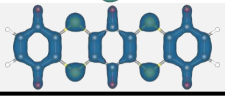	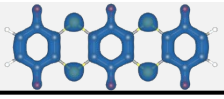	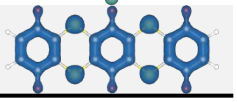

Table S9. HOMO-LUMO energy level diagrams of 25PBQS, 25PBQS^{2-}, 25PBQS^{4-} and 25PBQS^{6-}.

Molecule	*HOMO*	*LUMO*
25PBQS	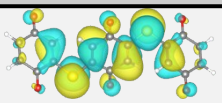 −6.82 eV	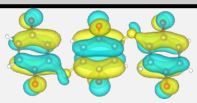 −4.07 eV
25PBQS^{2-}	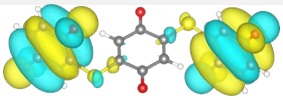 −4.41 eV	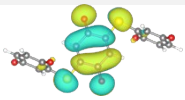 −2.92 eV
25PBQS^{4-}	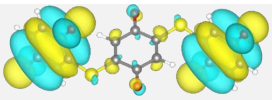 −1.84 eV	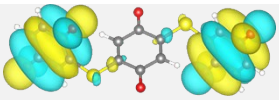 −1.54 eV
25PBQS^{6-}	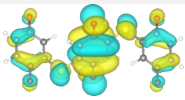 −0.95 eV	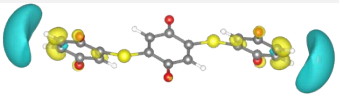 −2.00 eV

Table S10. HOMO-LUMO energy level diagrams of **2**6PBQS, 26PBQS^{2-}, 26PBQS^{4-} and 26PBQS^{6-}.

Molecule	*HOMO*	*LUMO*
26PBQS	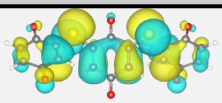 −6.91 eV	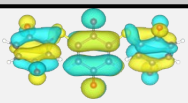 −4.15 eV
26PBQS^{2-}	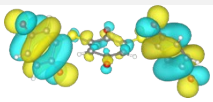 −4.13 eV	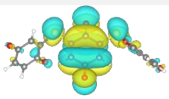 −2.97 eV
26PBQS^{4-}	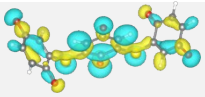 −1.84 eV	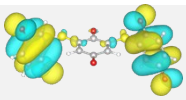 −1.58 eV
26PBQS^{6-}	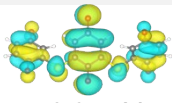 −0.97 eV	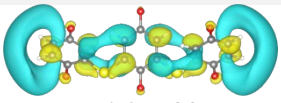 −1.97 eV

Table S11. HOMO-LUMO energy level diagrams of 2356PBQS, $2356PBQS^{2-}$, $2356PBQS^{4-}$ and $2356PBQS^{6-}$.

Molecule	*HOMO*	*LUMO*
2356PBQS	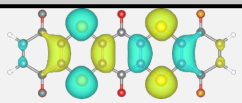 −6.02 eV	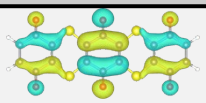 −4.41 eV
2356PBQS^{2-}	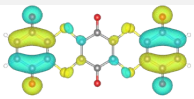 −4.07 eV	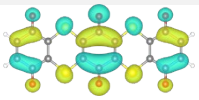 −3.09 eV
2356PBQS^{4-}	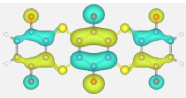 −2.07 eV	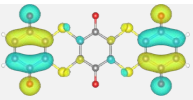 −1.33 eV
2356PBQS^{6-}	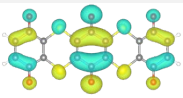 −0.93 eV	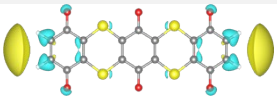 −1.95 eV

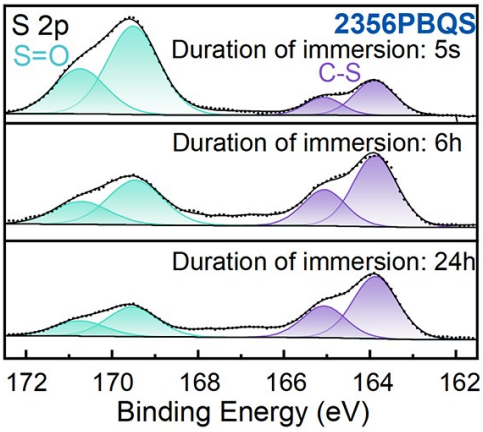

Fig. S22. S 2p XPS spectra of 2356PBQS cathode cycled in $Mg(TFSI)_2$-$MgCl_2$/DME electrolyte, showing the effect of soaking duration (5 s, 6 h, and 24 h) on the S 2p XPS spectra in the discharge state.

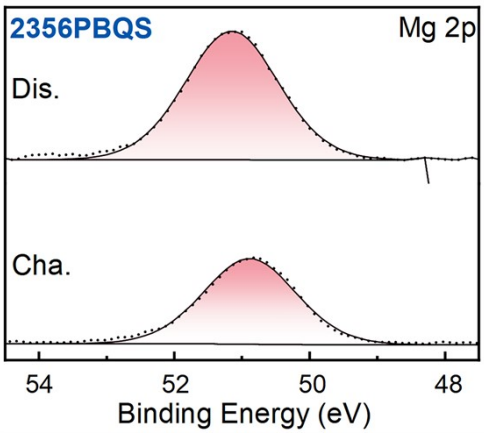

Fig. S23. Mg 2p XPS spectra of 2356PBQS at the charge/discharge states with $Mg(TFSI)_2$-$MgCl_2$/DME electrolyte.

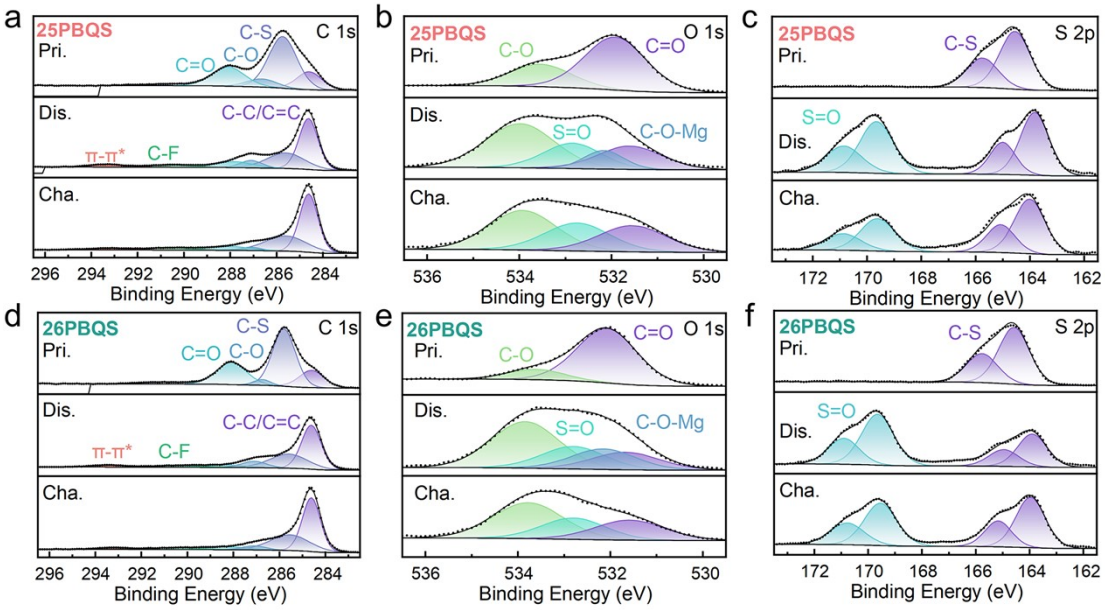

Fig. S24. XPS spectra of (a–c) 25PBQS and (d–f) 26PBQS at the charge and discharge states of the 4th cycle with $Mg(TFSI)_2$-$MgCl_2$/DME electrolyte.

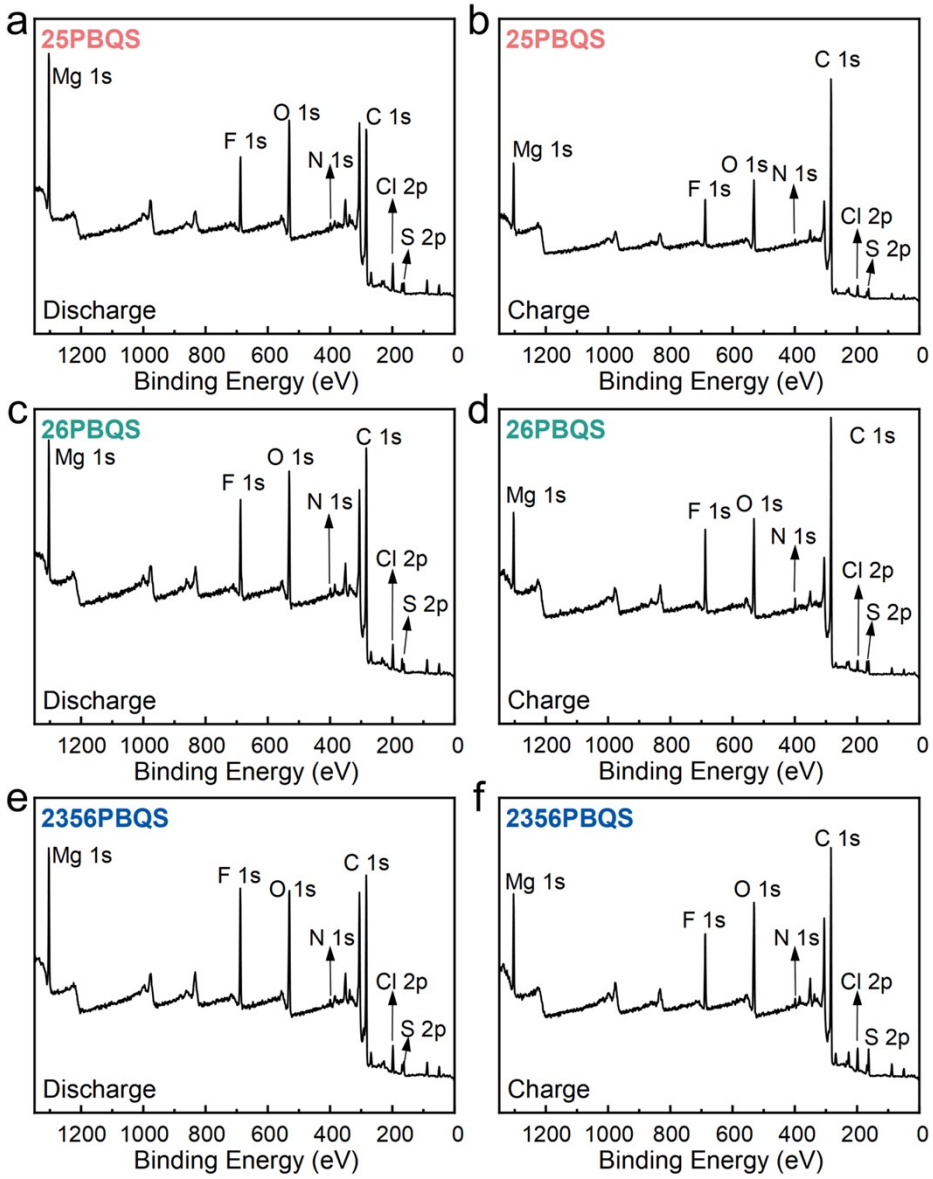

Fig. S25. XPS spectra of (a–b) 25PBQS, (c–d) 26PBQS, and (e–f) 2356PBQS at discharge and charge states of the 4th cycle with $Mg(TFSI)_2$-$MgCl_2$/DME electrolyte.

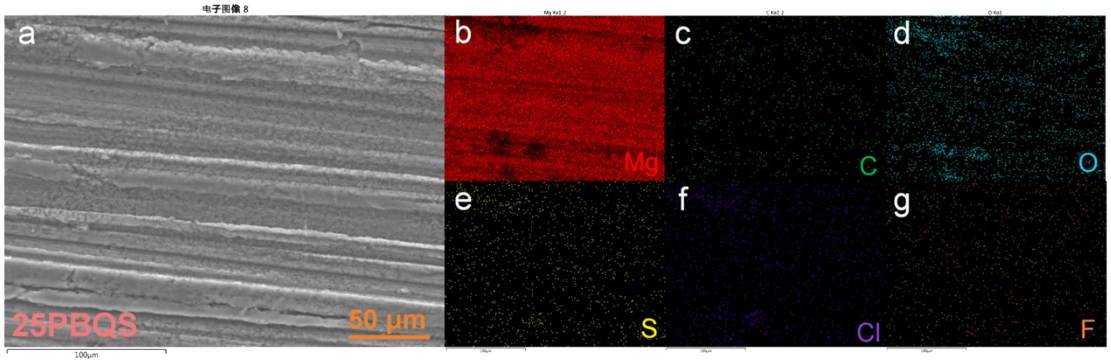

Fig. S26. (a) SEM image and (b–g) EDS elemental mapping of the Mg anode from a Mg‖25PBQS cell after 6 cycles.

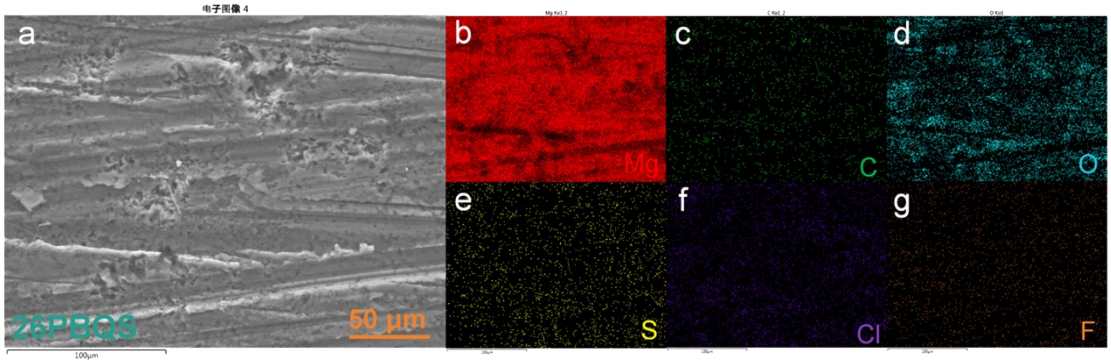

Fig. S27. (a) SEM image and (b–g) EDS elemental mapping of the Mg anode from a Mg‖26PBQS cell after 6 cycles.

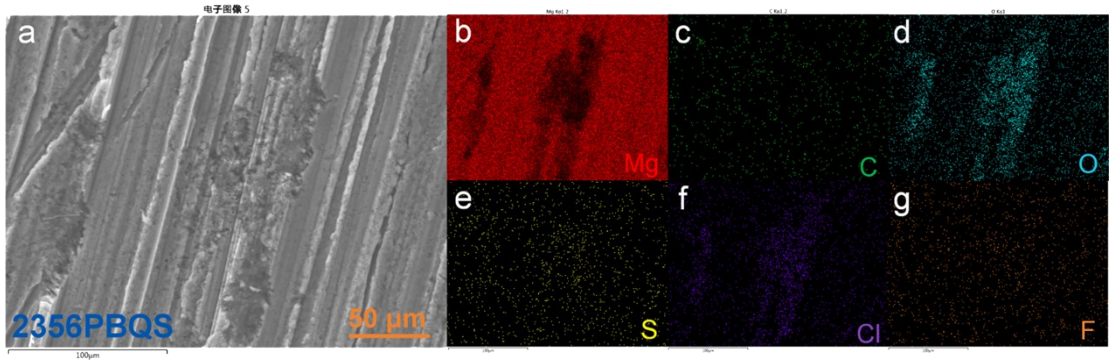

Fig. S28. (a) SEM image and (b–g) EDS elemental mapping of the Mg anode from a Mg‖2356PBQS cell after 6 cycles.

Table S12. Energy (a.u.) comparison in the singlet, triplet and quintet.

Molecule	*Singlet*	*Triplet*	*Quintet*
25PBQS^{2-}	−1939.105318	−1939.118947	/
25PBQS^{4-}	−1939.291984	−1939.296557	−1939.225335
25PBQS^{6-}	−1939.377896	−1939.317704	−1939.240841
26PBQS^{2-}	−1939.102057	−1939.116264	/
26PBQS^{4-}	−1939.291582	−1939.295255	−1939.226940
26PBQS^{6-}	−1939.377691	−1939.315234	−1939.238085
2356PBQS^{2-}	−2733.150036	−2733.153560	/
2356PBQS^{4-}	−2733.341925	−2733.343031	−2733.276925
2356PBQS^{6-}	−2733.428806	−2733.357194	−2733.282077
25PBQS-Mg	−2339.316012	−2339.347076	−2339.263327
2356PBQS-Mg	−9399.168073	−9400.320168	−9400.317367

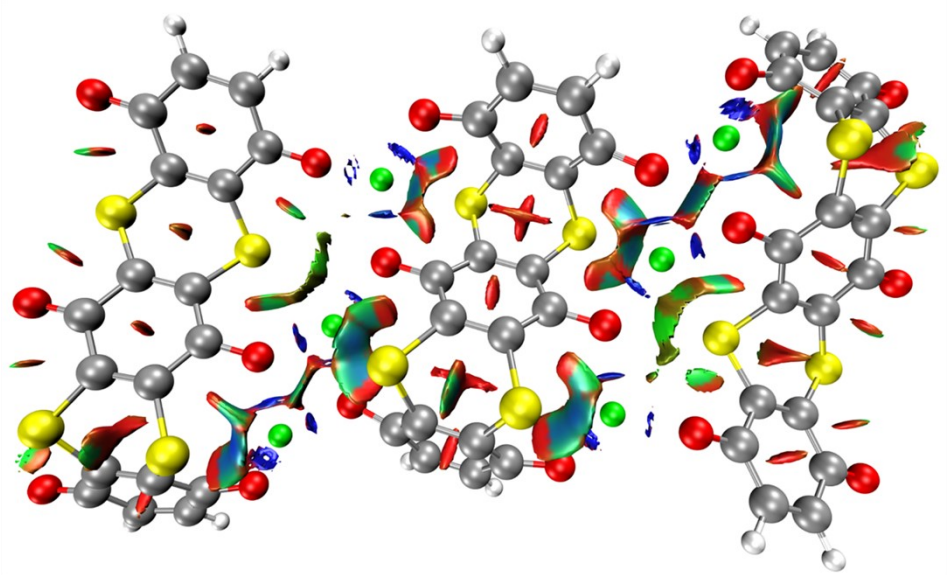

Fig. S29. Reduced density gradient (RDG) isosurfaces (s = 0.5 au) for 2356PBQS-Mg. The surfaces are colored on a blue-green-red scale according to values of sign(λ_2)ρ, ranging from −0.035 to 0.02 au. Blue indicates strong attractive interactions, and red indicates strong nonbonded overlap.

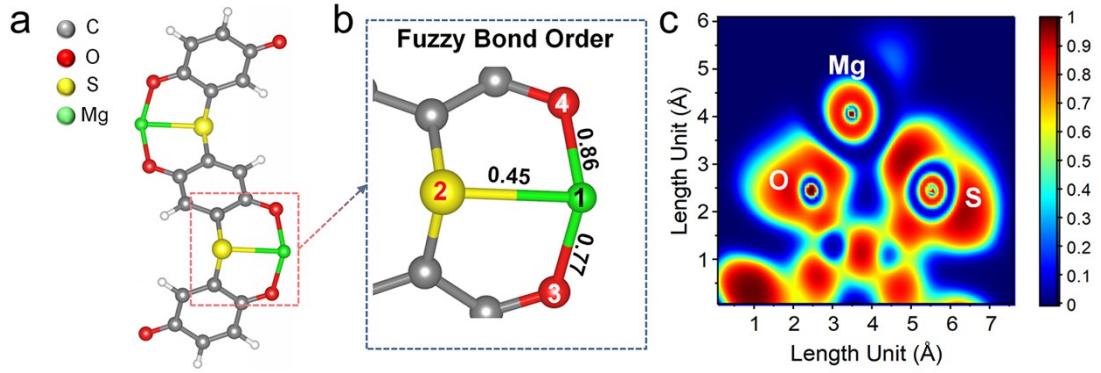

Fig. S30. (a) Molecular structure; (b) Partial view of the molecular structure with fuzzy bond orders and (c) ELF of 25PBQS-Mg (Mg1, S2 and O4).

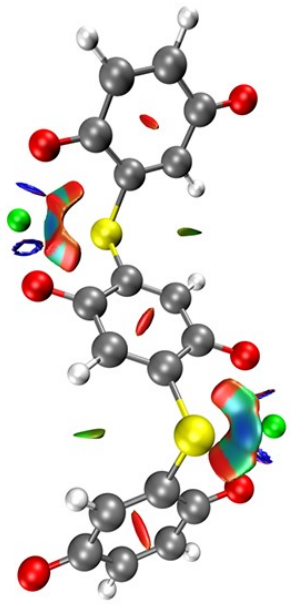

Fig. S31. RDG isosurfaces (s = 0.5 au) for 25PBQS-Mg. The surfaces are colored on a blue-green-red scale according to values of sign(λ_2)ρ, ranging from −0.035 to 0.02 au.

References:

[1] N. Tran, J. Leprêtre and F. Alloin, *Electrochim. Acta*, 2021, **375**, 137990. DOI: 10.1016/j.electacta.2021.137990.

[2] G. Dawut, Y. Lu, L. Mao and J. Chen, *Inorg. Chem. Front.*, 2018, **5**, 1391-1396. DOI: 10.1039/c8qi00197a.

[3] Z. Song, Y. Qian, T. Zhang, M. Otani and H. Zhou, *Adv. Sci.*, 2015, **2**, 1500124. DOI: 10.1002/advs.201500124.

[4] X. Ren, D. Tao, S. Cui, T. Li, Y. Cao and F. Xu, *Energy Storage Mater.*, 2023, **63**, 102992. DOI: 10.1016/j.ensm.2023.102992.

[5] B. Pan, J. Huang, Z. Feng, L. Zeng, M. He, L. Zhang, J. T. Vaughey, M. J. Bedzyk, P. Fenter, Z. Zhang, A. K. Burrell and C. Liao, *Adv. Energy Mater.*, 2016, **6**, 1600140. DOI: 10.1002/aenm.201600140.

[6] X. Ren, F. Wen, S. Cao and F. Xu, *Chem. Eng. J.*, 2023, **452**, 139570. DOI: 10.1016/j.cej.2022.139570.

[7] Z. Hu, L. Huang, X. Gan, Y. Han, J. Chu and Z. Song, *ACS Appl. Mater. Interfaces*, 2024, **16**, 19014-19025. DOI: 10.1021/acsami.4c02399.

[8] Y. Ding, X. Ren, D. Chen, F. Wen, T. Li and F. Xu, *ACS Appl. Energy Mater.*, 2022, **5**, 3004-3012. DOI: 10.1021/acsaem.1c03652.

[9] S. Cui, T. Li, D. Tao, D. Zhang, Y. Cao and F. Xu, *Energy Storage Mater.* 2024, **71**, 103672. DOI: 10.1016/j.ensm.2024.103672.

[10] Y. Wang, Z. Liu, C. Wang, Y. Hu, H. Lin, W. Kong, J. Ma and Z. Jin, *Energy Storage Mater.*, 2020, **26**, 494-502. DOI: 10.1016/j.ensm.2019.11.023.

[11] D. Tao, T. Li, Y. Tang, H. Gui, Y. Cao and F. Xu, *Adv. Funct. Mater.*, 2024, **34**, 2411223. DOI: 10.1002/adfm.202411223.

[12] X. Xue, R. Chen, X. Song, A. Tao, W. Yan, W. Kong and Z. Jin, *Adv. Funct. Mater.*, 2021, **31**, 2009394. DOI: 10.1002/adfm.202009394.

[13] D. Tao, L. Ran, T. Li, Y. Cao and F. Xu, *ACS Nano*, 2024, **18**, 28810-28821. DOI: 10.1021/acsnano.4c08576.

[14] H. Dong, Y. Liang, O. Tutusaus, R. Mohtadi, Y. Zhang, F. Hao and Y. Yao, *JOULE*, 2019, **3**, 782-793. DOI: 10.1016/j.joule.2018.11.022.